Phase separation enables heterochromatin domains to do mechanical work

Jessica F. Williams[1], Ivan V. Surovtsev[1], Sarah M. Schreiner[1], Hang Nguyen[1], Yan Hu[1], Simon G.J. Mochrie[2], and Megan C. King[1]*

[1] Department of Cell Biology, Yale School of Medicine, 333 Cedar Street, New Haven, Connecticut, USA, 06520

[2] Department of Physics, Department of Applied Physics, Yale University, 217 Prospect Street, New Haven, Connecticut, USA, 06511

* Lead Contact and to whom correspondence should be addressed: megan.king@yale.edu

Summary

Liquid-liquid phase separation (LLPS) has emerged as a major driver of cellular organization. However, it remains unexplored whether the mechanical properties of LLPS domains are functionally important. The heterochromatin protein HP1-α (and the orthologous Swi6 in *S. pombe*) is capable of LLPS *in vitro* and promotes formation of LLPS heterochromatin domains *in vivo*. Here, we demonstrate that LLPS of Swi6 contributes to the emergent mechanical properties of nuclei. Using nuclear fluctuation analysis in live cells and force spectroscopy of isolated nuclei, we find that disrupting histone H3K9 methylation or depleting Swi6 compromises nuclear stiffness, while heterochromatin spreading through loss of the H3K9 demethylase, Epe1, increases nuclear stiffness. Leveraging a separation-of-function allele, we demonstrate that phase separation of Swi6—but not its histone binding or dimerization—is essential for Swi6's mechanical role. These findings demonstrate that altering chromatin state has mechanical consequences and highlights that phase-separated domains can do mechanical work.

Introduction

The cell nucleus plays a vital role in protecting the genome from external sources of damage including mechanical force and DNA degrading enzymes. The main component of the nucleus that shields the genome from these stressors is its nuclear envelope, an integrated network of the inner and outer nuclear membranes, peripheral heterochromatin, nuclear pore complexes, integral inner nuclear membrane proteins, and, in higher eukaryotes, a polymer mesh of intermediate filaments (lamins). Maintaining the integrity of the nuclear envelope is critical for cell survival, and mechanical defects that lead to nuclear blebbing and rupture not only are sources of DNA damage but are also linked to human disease (Lusk and King, 2017; Shah et al., 2017). Ruptures can occur during cellular migration, when cells move through tissue and experience significant compressive forces (Denais et al., 2016; Raab et al., 2016), but intrinsic cytoskeletal forces in adherent cells are also strong enough to induce nuclear ruptures, indicating the nucleus is under constant strain induced by its own cellular architecture (Hatch and Hetzer, 2016; Vargas et al., 2012).

In the quest to understand how the nucleus withstands mechanical forces, most work has focused on the effect of the nuclear lamina (Harada et al., 2014; Lammerding et al., 2006). However, we previously demonstrated that chromatin, by means of its tethering to the nuclear envelope, makes critical contributions to the stiffness of the nucleus in fission yeast, which lack nuclear lamins (Schreiner et al., 2015). Further studies in mammalian cells demonstrated that chromatin contributes to the nuclear force response to small deformations (1-3 μm), while A-type lamins are critical for the force response to large deformations (> 3 μm) (Stephens et al., 2017). Global chromatin compaction also has mechanical consequences (Furusawa et al., 2015). Thus, both the lamina and the underlying chromatin are important for maintaining mechanical stability, yet each play separate roles related to the scale of the external strain. Strikingly, increasing the amount of heterochromatin is sufficient to rescue the nuclear irregularity and nuclear blebbing phenotype seen in HeLa cells expressing the mutant form of lamin A (progerin)

of the premature aging disease Hutchinson-Guilford Progeria Syndrome (Stephens et al., 2018). Recent work also demonstrates that histone deacetylase 3 is shuttled into the nucleus in response to compressive force, where it activates an increase in heterochromatin (Damodaran et al., 2018). Together, these studies suggest that in addition to functioning as a transcriptional insulator (Bickmore and van Steensel, 2013), heterochromatin likely plays an additional mechanical role to support the nucleus (Bustin and Misteli, 2016).

An evolutionarily conserved feature of nuclear organization is the association of heterochromatin with the nuclear periphery (Towbin et al., 2013). This localization has classically been thought to reflect the ability of heterochromatin to promote gene silencing. Recent studies, however, have called this model into question. In *C. elegans*, heterochromatin positioning at the nuclear periphery does not dictate gene silencing (Gonzalez-Sandoval and Gasser, 2016). Moreover, leveraging the model of rod cells with “inverted” nuclei, re-localization of heterochromatin from the periphery to the center of the nucleus has been found to alter neither gene expression nor chromatin organization (Falk et al., 2019). An alternative model, tested here, is that the peripheral localization of heterochromatin instead reflects its importance in mechanically supporting the nuclear envelope. Indeed, our previous work has shown that heterochromatin at the nuclear periphery—specifically its association with spindle pole bodies through centromeric heterochromatin—is important for resisting the microtubule forces (King et al., 2008; Schreiner et al., 2015). Until now, the physical basis for the unique mechanical property that heterochromatin imparts on the nucleus has remained undetermined.

One hypothesis for how heterochromatin could contribute to the mechanical stiffness of the nucleus involves recent evidence that a key protein responsible for heterochromatin compaction and gene silencing—heterochromatin protein (HP1α)—forms phase-separated, HP1α-rich heterochromatic domains (Larson et al., 2017; Strom et al., 2017). These (and other) liquid-liquid phase-separated (LLPS) domains found in cells exhibit

liquid-like properties, including surface tension and viscosity (Berry et al., 2015; Brangwynne et al., 2009; 2011; Elbaum-Garfinkle et al., 2015; Molliex et al., 2015; Zhang et al., 2015). In one model, we can imagine that the surface tension of LLPS heterochromatic domains, which can be enhanced by strong electrostatic interactions between elements of the liquid(s) as observed for HP1α (Larson and Narlikar, 2018; Weinbreck et al., 2008), would resist deformation. Alternatively or in addition, a distinct model of "elastic ripening" (Rosowski et al., 2020) is being developed, in which synthetic LLPS domains embedded in polymer networks form a composite system with emergent mechanical properties separate from the effects of surface tension. Importantly, while it has been proposed that phase separation can do mechanical work in an artificial system by bringing two chromatin loci together (Shin et al., 2018), whether this attribute serves a biological function has yet to be tested.

Here, we show that the existence and scale of HP1-α/Swi6 phase-separated domains strongly contribute to nuclear stiffness in *S. pombe*. We find that disrupting H3K9 methylation or depleting HP1-α/Swi6 results in decreased nuclear stiffness, while loss of the H3K9 demethylase, KDM2/Epe1, increases nuclear stiffness. A separation-of-function allele reveals that the ability of Swi6 to undergo phase separation, rather than its H3K9me binding or dimerization, is critical for its mechanical contribution. Taken together, our results support the hypothesis that phase-separated systems can do mechanical work, which cells leverage to support the mechanical integrity of the nucleus.

Results

Loss of HP1-α/Swi6 enhances nuclear deformability *in vivo.*

In fission yeast, H3K9me-rich heterochromatin is primarily located at the centromeres and telomeres, which are positioned at the nuclear periphery. At the periphery, the centromeric heterochromatin is mechanically integrated with the nuclear envelope at the site of the spindle pole body (SPB) attachment. In this context, shear forces originating by polymerizing microtubule (MT) bundles push the SPB and the coupled centromeric heterochromatin, deforming the nuclear envelope (King et al., 2008; Schreiner et al., 2015) (**Fig. 1A**). This characteristic local deformation thus allows one to monitor the nuclear force response to intrinsic perturbations. To evaluate the size of these nuclear deformations, the nuclear envelope was labeled by expression of a GFP fusion of the nucleoporin Cut11 and visualized in all four-dimensions (4D: x, y, z, and time) by live-cell fluorescence microscopy (**Fig. 1B**). 4D microscopy allows for precise spatial and temporal resolution of the nuclear envelope as we monitor deformations in the surface contour. To quantify these deformations, we employed a three-dimensional (3D) surface reconstruction software previously developed in our labs (Schreiner et al., 2015; Zhao et al., 2016). This method uses a series of fluorescent z-stacks to reconstruct the nuclear envelope surface in 3D with sub-pixel resolution (**Fig. 1C**). Time-lapse surface changes are tuned to detect fluctuations of 25 nm or larger, which sufficiently captures intrinsic MT-driven deformations and thus can be used as a proxy for the *in vivo* nuclear response to these MT forces. Larger fluctuations suggest the ability of the nuclear envelope (NE) to deform and bend; under the same forces, smaller fluctuations suggest resistance to deformation (stiffness). For individual nuclei the largest fluctuations manifest at the points subject to shear forces as MTs drive SPB oscillations, which can be visualized as local maxima on the nuclear surface (**Fig. 1B-D**); these maxima are lost upon MT depolymerization with the drug carbendazim (MBC). When averaged over many nuclei, the largest fluctuations occur at ~45 and 135 degrees with respect to the

long axis of the cell—the points at which the SPB is maximally translated due to the shearing force from the MTs (**Fig. 1F**).

We first examined the mechanical contribution of the heterochromatin protein HP1-α/Swi6 to this *in vivo* nuclear response to MT forces. As HP1-α/Swi6 is a key component of centromeric and telomeric heterochromatin, responsible for its condensation and transcriptional repression (Allshire et al., 1995; Ekwall et al., 1995; Lorentz et al., 1994) and has recently been shown to oligomerize and form phase-separated domains that facilitate heterochromatin formation (Canzio et al., 2011; Larson et al., 2017; Strom et al., 2017), we hypothesized that HP1-α/Swi6's ability to organize chromatin might also impart mechanical support to the NE (**Fig. 1E**). Indeed, in individual cells lacking Swi6 we observed larger nuclear fluctuations at the characteristic locations (**Fig. 1D**), suggesting that loss of Swi6 does not affect the NE-SPB architecture but instead reduces the ability of the nucleus to resist MT forces. Averaging over hundreds of nuclei, the locations of the fluctuations in *swi6Δ* cells mirrored the wild-type profile, but was shifted up toward larger fluctuations (**Fig. 1F**). When compared to wild-type cells, *swi6Δ* cells displayed larger fluctuations at all angles (**Fig. 1F**), as reflected in the root mean squared fluctuation size in both the presence and absence of MT dynamics (**Fig. 1G**). Thus, when Swi6 is present, it contributes to resisting these nuclear deformations.

We were unable to assess the effect of disrupting H3K9me by genetic deletion of the H3K9 methylase, Suv39/Clr4, as we observed disrupted MT-nuclear dynamics (i.e., loss of the characteristic nuclear radial fluctuation profile) in *clr4Δ* cells (**Supp. Fig. S1A-B**) (King et al., 2008). However, *clr4Δ* nuclei exhibited larger membrane fluctuations than wild-type cells when MTs were depolymerized by the addition of MBC (**Supp. Fig. S1B**), suggesting that *clr4Δ* nuclei may be more deformable. We next evaluated the mechanical effects of expanding heterochromatic domains by deletion of the H3K9me2/3 demethylase, KDM2/Epe1 (**Fig. 1E**). Loss of Epe1 has been shown to promote spreading of H3K9 heterochromatin outside of its normal chromatin regions,

enlarging the size of heterochromatic domains (Wang et al., 2015; Zofall and Grewal, 2006). Despite this, we observed no significant difference in nuclear envelope fluctuation size in Epe1-deficient nuclei as compared to wild type *in vivo* (**Fig. 1D,F-G**), suggesting that even in the presence of larger heterochromatin domains, the nucleus maintains its normal response to MT shearing force.

H3K9me-associated Swi6 strongly contributes to nuclear stiffness *in vitro*.

Assessing nuclear mechanics by monitoring nuclear envelope fluctuation size in response to intrinsic cytoskeletal forces *in vivo* is not a direct mechanical measurement and can only reflect the response to shear forces exerted on the SPB. However, in other contexts, for example in mammalian tissues or migrating cells, the nucleus is also likely to be subjected to tension and compression forces. To directly interrogate how fission yeast nuclei respond to explicit magnitudes, time scales, and a compression/tension regime, we employed an *in vitro* force spectroscopy approach on isolated nuclei that we developed previously (Schreiner et al., 2015) to directly measure the effect of altering H3K9me levels and depleting Swi6 on nuclear stiffness.

Nuclei expressing Cut11-GFP were isolated and used to perform single-nuclei force spectroscopy measurements using optical tweezers (**Fig. 2A-B**). To directly measure its mechanics, a nucleus was sandwiched between two silica beads, a larger bead adherent to a glass slide with the other, smaller bead trapped in the optical trap (**Fig. 2A-B**). As the larger bead was moved by a piezo stage ($\Delta x_{\text{piezostage}}$), the displacement of the smaller bead in the trap was measured (Δx_{bead}); the difference in x-displacement is the amount by which the nucleus was either stretched or compressed ($\Delta x_{\text{nucleus}}$). Similar to our previous work, we treated the system as a spring and used the displacement and the force required to calculate the effective spring constant—or stiffness—of the individual nucleus (Schreiner et al., 2015) (**Fig. 2C**). Each nucleus was subjected to multiple rounds of tension and compression at varying time scales, with all oscillations

performed over a range of biologically-relevant frequencies: 0.01 Hz – 2 Hz (**Supp. Fig. S3**).

The nuclear response to compression and tension forces *in vitro* revealed pronounced mechanical effects when heterochromatin formation was perturbed. Loss of KDM2/Epe1, which leads to heterochromatin spreading, resulted in increased nuclear stiffness, while loss of either the Suv39/Clr4 H3K9 methylase or HP1-α/Swi6, which respectively leads to loss of H3K9me heterochromatin domain formation or compaction, led to a substantial reduction in nuclear stiffness (**Fig. 2D**). Thus, the extent and composition of heterochromatin has a strong effect on the nuclear force response to compression and tension. At longer oscillation frequencies (100 s or 0.01 Hz), we observed a characteristic reduction in effective stiffness, or non-linear mechanical response, in wild-type, *clr4Δ*, and *swi6Δ* nuclei, indicating that these systems are not perfect springs but instead combinations of an elastic spring and a viscous dashpot, or dampener. To extract these individual mechanical properties of nuclear stiffness and viscosity, we performed non-linear regression applying the Maxwell viscoelastic model to our frequency series of effective stiffnesses (Schreiner et al., 2015) (**Fig. 2D**). The actual stiffness followed the same trend as the effective stiffness, further highlighting the critical effect of perturbing Epe1, Clr4, or Swi6 on nuclear stiffness (**Fig. 2E**). Loss of Epe1 also led to a significant increase in nuclear viscosity, so large that it was unable to be determined from the timescales sampled with our oscillation assay (**Fig. 2F**). Conversely, loss of Clr4 or Swi6 led to a decrease in nuclear viscosity, suggesting a more fluid-like system with more chromatin flow (**Fig. 2F**). Taken together these results indicate the substantial mechanical effect of perturbing H3K9me heterochromatin quantity and its properties has on the nucleus (**Fig. 2G**). Without the ability to form normal H3K9me heterochromatin domains, either through loss of H3K9 methylation or Swi6-mediated condensation, nuclei become softer and less viscous. When heterochromatin domains expand, however, the nucleus not only becomes more stiff, but also significantly more viscous, resembling more of a solid-like substance on this time scale.

Heterochromatic domains exhibit liquid-liquid phase separation properties *in vivo* that promote telomere clustering

In light of the significant mechanical defects we observed in the absence of Swi6, we next sought to interrogate the mechanism by which Swi6 provides mechanical support. Building on previous work that has characterized the liquid-like behavior of *S. pombe* Swi6 *in vitro* (Canzio et al., 2011; 2013; Sanulli et al., 2019) as well as *in vivo* observations of HP1-α in mammalian cells comprising an apparent mobile "phase" around otherwise immobile heterochromatin foci (Larson et al., 2017; Strom et al., 2017), we hypothesized that the ability of Swi6 to undergo phase separation could influence the organization of heterochromatin in fission yeast, which, in turn, could affect the mechanics of the nucleus. In line with previous LLPS studies, we too observed a reduction in Swi6-labeled heterochromatin foci size and intensity when treated with the phase-disrupting solvent 1,6-hexanediol (**Supp. Fig. S4**). With this in mind, we first sought to further characterize the LLPS properties of Swi6 at two regions at which it is highly enriched: the centromeres and the telomeres (Ekwall et al., 1995; Kanoh et al., 2005; Nakayama et al., 2001).

When Swi6 is visualized as a fluorescent protein fusion expressed from its endogenous locus (Swi6-GFP), it resides in several nuclear foci/domains (**Fig. 3A-B**). The largest domain is comprised of the three centromeres, which are coupled to the SPB interface and subjected to MT-dependent force transmission. The other, smaller heterochromatic foci contain the six telomeres, the mating type locus, and other silenced regions of the genome. As the centromeric heterochromatin is driven across the nucleus, we frequently observe that it undergoes a transition from being predominantly circular when "at rest" (at t = 0) to being stretched along the SPB oscillation axis (at t = 30-70s), sometimes displaying an apparent fission into smaller, individual domains (after t = 60s) (**Fig. 3B**). This observation reinforces that mechanical force is transduced to the

heterochromatin, leading to changes in domain morphology. These observations are consistent with a model in which a heterochromatic domain can act as a mechanical cushion, absorbing a portion of the MT-driven forces exerted upon the nucleus through its own resistance to deformation and/or its effects on the emergent properties of the chromatin itself. Furthermore, the force response of the Swi6-containing heterochromatic domain is consistent with liquid-like reorganization (undergoing droplet fission and fusion). Moreover, consistent with previous observations for HP1-α in mammalian cells (Strom et al., 2017), the addition of 5% of the aliphatic alcohol 1,6-hexanediol, which disrupts weak hydrophobic interactions, led to a decrease in both the size and intensity of GFP-Swi6 foci and the accumulation of a diffuse pool of GFP-Swi6 throughout the cell (**Supp. Fig. S4**).

Another unique property of LLPS systems is their ability to undergo fusion (Alberti et al., 2019; Brangwynne et al., 2011). Heterochromatin domains coalesce in *S. pombe*; for example, the six (replicated) telomeres cluster together at the nuclear periphery (Gasser et al., 2004). When visualized by expressing a GFP fusion of Taz1, a shelterin complex subunit that specifically binds telomeric DNA (Cooper et al., 1998), we typically observe a range of 1-4 telomere cluster foci with approximately half of nuclei displaying one or two foci containing the 6 telomeres, indicating prior fusion events into larger telomere clusters (**Fig. 3C,E**). This behavior is consistent throughout the cell cycle, as assessed by using cell length as a proxy for cell cycle progression (**Fig. 3E**). Consistent with these clusters representing phase-separated domains, treatment with 1,6-hexanediol (5% for 30 minutes) resulted in an increase in the number of Taz1-GFP foci per nucleus—particularly in the G2 phase of the cell cycle—suggesting that LLPS could promote telomere clustering in fission yeast (**Fig. 3D-E**) as has been suggested recently for telomeres in other contexts (Zhang et al., 2020). We next asked if Swi6 is required for telomere clustering. Indeed, we found that, like 1,6-hexanediol treatment, *swi6Δ* cells had an increase in the number of Taz1-GFP foci per nucleus (**Fig. 3E**). We note that even in this condition many cells display less than 6 discernible telomere foci. We suspect that this occurs due to stochastic coincidence of telomeres in the nuclear

volume or an inability to fully visualize the dimmer, de-clustered telomeres. Taken together, these observations suggest the possibility that Swi6's ability to undergo LLPS is necessary for normal telomere clustering in fission yeast.

Swi6 is a unique heterochromatin protein with a mechanical function

In fission yeast, Swi6 shares its transcriptional silencing role in gene regulation with other chromodomain proteins, including Chp1 and Chp2, which are necessary for the proper establishment and balance of heterochromatic regions, respectively (Sadaie et al., 2004; 2008). All three chromodomain proteins rely on the methylase Clr4 to be recruited to methylated histones of heterochromatic domains (Haldar et al., 2011; Sadaie et al., 2004). However, their protein structures differ from each other, with Chp1 lacking a chromo-shadow domain and containing a much smaller N-terminal domain (Sadaie et al., 2004) (**Fig. 4A**). An open question is if and how this family of proteins compete for methylated H3K9 binding sites as well as what are their respective contributions to the physical properties of heterochromatic domains. To address this, we visualized Chp1-GFP under a number of conditions (**Fig. 4B**). We first verified that Chp1—like Swi6—is unable to bind and localize to heterochromatic foci in the absence of Clr4 (Sadaie et al., 2004) (**Fig. 4C**). Interestingly, we observed evidence for competition for H3K9me binding, as cells lacking Swi6 had a significant increase in Chp1-GFP foci intensity (**Fig. 4D, F**). Importantly, increased occupancy of Chp1 in the absence of Swi6, could not compensate Swi6's mechanical contribution or telomere clustering function (**Figs. 1D, F-G, 2D-F, 3E**), indicating that Swi6 is unique in its organization of heterochromatin and mechanical functions. When heterochromatin was allowed to spread due to the absence of Epe1, we also observed that Chp1-GFP intensity increased at heterochromatic foci, but to a lesser extent (**Fig. 4E-F**), consistent with both the enlargement of heterochromatin domains in Epe1-deficient cells and the competition with Swi6 (**Fig. 4G**). These observations underscore the effect of the

heterochromatin perturbations explored here and also provide evidence for competition between non-equivalent H3K9me binding proteins at heterochromatic domains.

The *swi6-sm1* allele uncouples H3K9me2/3 binding from phase separation

To determine whether Swi6's abilities to bind, condense, and/or silence H3K9me heterochromatin are coupled to its ability to form phase-separated domains, we interrogated the *swi6-sm1* allele, which carries two mutations in its N-terminal domain, rendering it unable to silence heterochromatin while leaving its H3K9me-binding activity, dimerization, and cohesin interactions unaffected (Yamagishi et al., 2008) (**Fig. 5A**). In previous studies of Swi6, defects in N-terminal phosphorylation by casein kinase II also led to loss of transcriptional silencing (Shimada et al., 2009). Indeed the D21G mutation encoded in the *swi6-sm1* allele disrupts the casein kinase II recognition site for phosphorylation of serine 18: this site is phosphorylated *in vivo* and *in vitro* by casein kinase II, and its targeted mutation disrupts Swi6's ability to promote gene silencing (Shimada et al., 2009). As N-terminal phosphorylation enhances oligomerization leading to phase separation for both HP1α and Swi6, (Canzio et al., 2013; Larson et al., 2017), we hypothesized that the *swi6-sm1* allele disrupts Swi6's ability to undergo LLPS due to altered phosphorylation.

To test our hypothesis, we imaged cells expressing either Swi6-GFP or *swi6-sm1*-GFP to measure the size, intensity, and number of heterochromatin foci within each nucleus (**Fig. 5B**). To quantitatively compare foci size and intensity, we employed an image analysis approach previously established in our labs that uses image z-stacks to reconstruct heterochromatin foci with sub-pixel resolution (Zhao et al., 2016) (**Fig. 5C**). Comparing each foci's intensity to its cross-sectional area in an ensemble scatter plot revealed divergent populations in Swi6-GFP versus *swi6-sm1*-GFP-labeled heterochromatin (HC) (**Fig. 5D**). In wild-type cells, Swi6-GFP HC domains comprised a more uniform distribution of intensities ranging from bright (centromeric HC) to dim

(telomeric and other HC). Cells expressing *swi6-sm1*-GFP, however, displayed a depletion of intermediately intense HC foci, indicative of non-centromeric HC domain de-clustering. Indeed, expression of *swi6-sm1* also inhibited telomere clustering in a manner that recapitulates complete loss of Swi6 or treatment with 1,6-hexanediol (**Fig. 5E**). Together, these results show that the N-terminus of Swi6, in addition to being critical for proper gene silencing, is also necessary for intermediately-sized HC domains and telomere clustering, both of which we hypothesize arise by LLPS-driven fusion. As the *swi6-sm1* allele mimics other systems which lack LLPS (e.g., cells treated with hexanediol and *swi6Δ* cells) in its telomere clustering defect, it supports previous work showing that the N-terminus of Swi6 serves an essential role in the formation of phase-separated domains (Canzio et al., 2013; Larson et al., 2017). It furthermore acts as a potential link between HP1-α/Swi6 phase separation and transcriptional silencing.

The *swi6-sm1* allele uncouples the mechanical defects of *swi6Δ* nuclei *in vivo* and *in vitro*

Given that the *swi6-sm1* allele is (1) recruited normally to H3K9me2/3-containing nucleosomes ((Yamagishi et al., 2008) and **Fig. 5**), (2) supports normal centromeric cohesion (Yamagishi et al., 2008), but (3) displays altered LLPS-like properties (**Fig. 6A**), we next tested the mechanical effect of expressing the *swi6-sm1* allele on the nuclear force response using our *in vivo* microscopy and *in vitro* nuclear force spectroscopy assays. We hypothesized that the ability of *swi6-sm1* to support proper cohesin loading at the centromeric heterochromatin that is subjected to tangential MT forces might support a normal force response, while the LLPS property of Swi6 could contribute to the nuclear stiffness and viscosity in response to direct compression or extension forces. Indeed, distinct from our observations in *swi6Δ* cells, *swi6-sm1* cells were found to have normal nuclear membrane deformability at all radial angles in response to MT forces, which was confirmed by the size of the root mean squared fluctuations, which also appeared normal in scale (**Fig. 6B**). We noted, however, that

there was an increase in the size of nuclear fluctuations in *swi6-sm1* cells in the absence of MT forces that recapitulated that seen in *swi6Δ* cells (**Fig. 6B**), hinting that global nuclear mechanics could be affected. Consistent with this, isolated *swi6-sm1* nuclei exhibited mechanical defects nearly identical to that seen for *swi6*Δ nuclei in response to direct compression and extension forces (**Fig. 6C**). Despite the ability of *swi6-sm1* to bind H3K9-methylated chromatin, dimerize, and support normal cohesin recruitment, it was completely defective in its ability to contribute to the nuclear stiffness (**Fig. 6D**) or viscosity (**Fig. 6E**), highlighting the mechanical importance of the Swi6 N-terminal domain, which has been shown to regulate Swi6's ability to undergo LLPS (**Fig. 6F**).

Discussion

In an effort to understand the contribution of heterochromatin to nuclear mechanics, we combined the use of H3K9me-associated genetic variants with *in vivo* and *in vitro* biomechanical assays. Our results support a model in which the phase separation properties of the heterochromatin protein Swi6 contributes to nuclear elasticity and viscosity. We propose that the ensemble mechanics of the nucleus arise from a composite system (individual, LLPS heterochromatin domains enmeshed in the chromatin polymer) that has emergent properties, much like what is seen in aqueous foams (e.g., shaving cream) (Weaire and Hutzler, 1999). We suggest that this emergent property provides a mechanism by which LLPS can support the resistance of the nucleus to compression or tension forces that could apply to other LLPS systems, particularly those coupled to biological membranes such as the nuclear envelope.

Modulating the extent of H3K9me-rich heterochromatin demonstrates that it is both necessary for the normal nuclear force response and sufficient, when expanded due to the lack of the H3K9me3 demethylase, Epe1, to increase nuclear stiffness. Previously, we showed that the nucleus behaves as a viscoelastic material, exhibiting both liquid

and solid characteristics that are time-dependent (Schreiner et al., 2015). This dual nature allows the nucleus to resist deformation (elasticity/stiffness) while allowing for chromatin flow within the nucleus (viscosity). Increased nuclear viscosity by H3K9 heterochromatin domain enlargement implies restricted chromatin movement under these conditions. The nucleus, in essence, behaves as a purely elastic solid on the minutes timescale, where its internal contents (chromatin) are in a fixed state, deforming together without losing their respective order. This mechanical transformation has potential implications for those physiologic states where cells exhibit gains in repressive H3K9 methylation marks, suggesting that increases in H3K9 methylation not only act to repress transcription but also repress the fluid-like dynamics and interactions of chromatin.

Conversely, disruption of H3K9 heterochromatin destabilizes the nucleus, reducing both its ability to resist deformation and impede chromatin flow. Nuclei that lack the H3K9 methyltransferase, Clr4, cannot recruit heterochromatin-condensing proteins (including Swi6) and therefore fail to form heterochromatin domains. As a result, these nuclei become softer and less viscous. Destabilization also occurs when only Swi6 is removed, suggesting that the specific properties of Swi6 are necessary for the mechanical effects of H3K9me heterochromatin rather than a direct effect of H3K9 methylation levels. This also excludes the potential contribution of other H3K9me-binding heterochromatin proteins such as Chp1 and Chp2 to substantially impact nuclear mechanics, singling out Swi6 as both necessary and unique.

With respect to telomere clustering, loss of Swi6, expression of the *swi6-sm1* allele, or treatment with 1,6-hexanediol all lead to the same de-clustering phenotype, suggesting that phase separation drives coalescence of telomeric heterochromatin. As the *swi6-sm1* allele also confers a silencing defect despite normal recruitment to H3K9me regions (Yamagishi et al., 2008), it is tempting to speculate that phase separation and silencing are tied.

It is important to note that a recent study has called into question the biological importance of the ability of HP1-α to phase-separate *in vitro* on its *in vivo* function, for example the failure of HP1-α over-expression to increase the size of heterochromatic domains as predicted for simple LLPS systems (Erdel et al., 2020). However, the complexity of feedback within heterochromatin is rife with paradox, for example the requirement for siRNA transcription to drive chromatin compaction and silencing in fission yeast (Yamanaka et al., 2013). Indeed, Swi6 recruits the H3K9me demethylase Epe1 almost exclusively into heterochromatic domains (Zofall and Grewal, 2006), which would be expected to decrease available H3K9me and thereby delocalize H3K9me-engaged Swi6 molecules, likely short-circuiting the ability of elevated Swi6 levels to drive heterochromatin spreading. Moreover, the binding of HP1-α/Swi6 to H3K9me and its subsequent compaction of heterochromatin involves an integrated set of activities driven by its (1) chromodomain avidity, (2) dimerization, (3) engagement of nucleosome arrays, and (4) its phase separation properties, all of which make it challenging to arrive at mechanistic conclusions without clear separation-of-function mutants or through engineered systems (Erdel et al., 2020). For this reason, the *swi6-sm1* allele and others of its kind that disrupt specific functionalities will be essential in future studies.

Erdel et al., also found that chromocenters in mouse cells were refractory to loss of HP1-α. Interestingly, we find that the size (and recruitment of Swi6) to the centromeric heterochromatin domain (most analogous to chromocenters, which are rich in pericentromeric repeats (Probst and Almouzni, 2008)) is relatively unaffected by the *swi6-sm1* mutation, while non-centromeric regions such as telomeres are strongly influenced. Despite this, the *swi6-sm1* allele has a profound mechanical effect, arguing that its mechanical function is strongly dependent on the phase separation property of Swi6 while its recruitment, dimerization, and influence on cohesin is not sufficient to affect its mechanics. We note that the *swi6-sm1* allele also confers a silencing defect, suggesting that there are also functional consequences for heterochromatic domains that are not reflected in the cytology of the centromeric heterochromatin. Exploring whether elasticity rather than surface tension driven by an interface between viscosities

(Rosowski et al., 2020) plays a role in biological systems such as HP1-α/Swi6 and heterochromatic domains will be an exciting future direction.

Taken together, our results suggest that phase-separated heterochromatin domains are able to do mechanical work by resisting deformation by an external force, similar to the ability of phase-separated droplets to deform the polymer mesh in which they are embedded (Style et al., 2018). Thus, we have extended the roles for phase separation *in vivo* beyond cellular compartmentalization to include mechanical functions, expanding our perspective on the multi-faceted functionality of phase separation in cellular biology.

Acknowledgements

We thank members of the King, Mochrie, and Lusk laboratories for helpful discussions, commentary, and troubleshooting, in particular, Hao Yan, Elisa Rodriguez, Andrea Nguyen, and Patrick Lusk. We thank the Yeast Genome Resource Center at Osaka University and the many investigators who have deposited strains at this resource. This work was supported by the NIH Pre-doctoral Program for Cellular and Molecular Biology (T32GM00722343), the NSF (CMMI-1334406) and the Physical and Engineering Biology Program at Yale.

Author Contributions

Conceptualization, J.W. and M.K.; Data curation, J.W., I.S., and H.N.; Formal analysis, J.W., I.S., H.N., and M.K.; Funding acquisition, S.M. and M.K.; Investigation, J.W., I.S., S.S., Y.H., and M.K.; Methodology, J.W., I.S., S.M., and M.K.; Project administration, M.K.; Resources, S.M. and M.K.; Software, J.W., I.S., and H.N.; Supervision, S.M. and M.K.; Validation, J.W., I.S., and M.K.; Visualization, J.W., I.S., and M.K.; Writing – original draft, J.W. and M.K.; Writing – review & editing, J.W., I.S., S.S., H.N., Y.H., S.M., and M.K.

Declaration of Interests

The authors declare no competing interests.

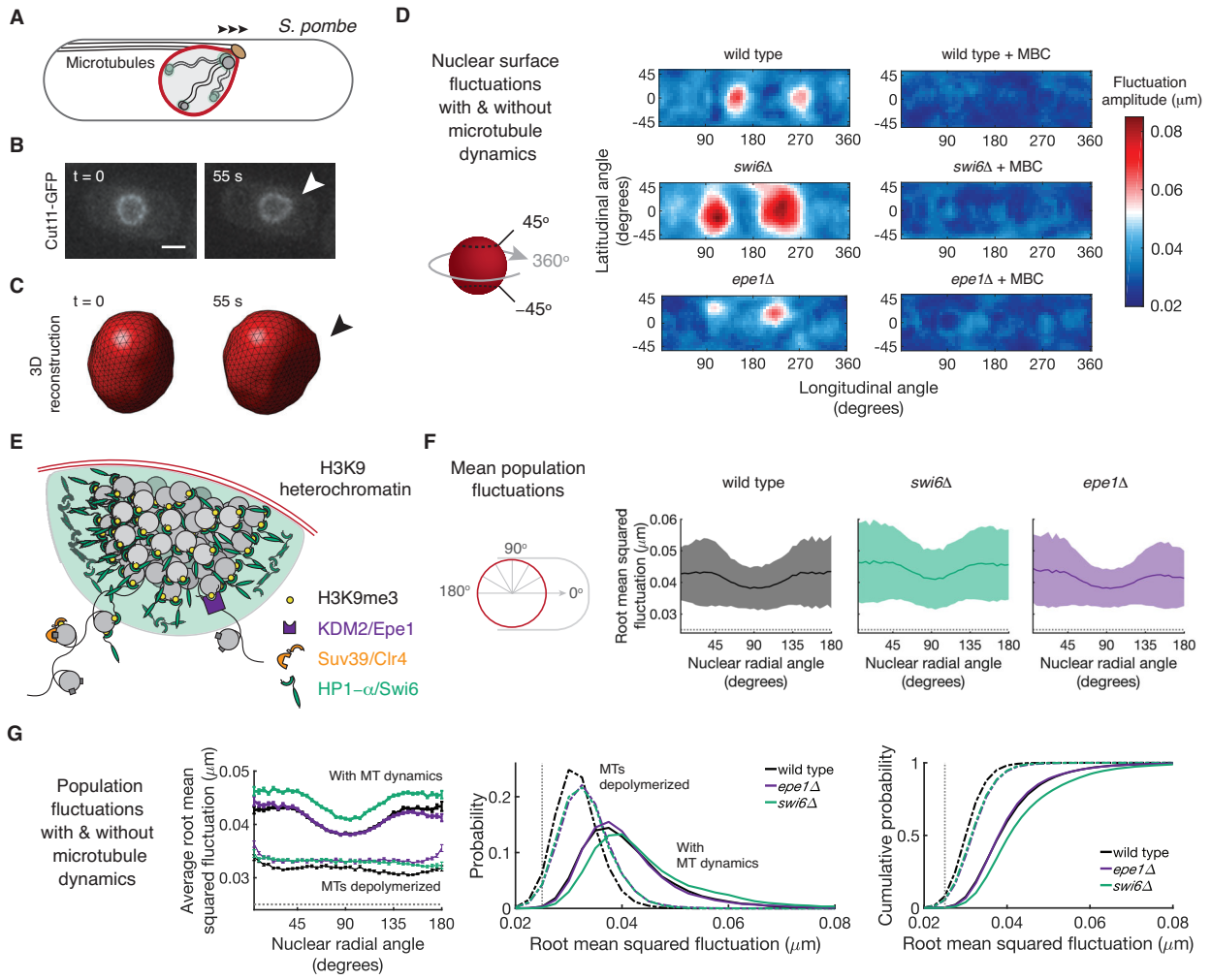

Figure 1. Loss of HP1-α/Swi6 enhances nuclear deformability *in vivo.*

Quantification of the intrinsic nuclear deformations in response to microtubule dynamics reveals larger nuclear envelope fluctuations in the absence of HP1-α/Swi6.

(A) In *S. pombe*, shearing forces acting upon the nucleus (red) arise from polymerizing microtubules (MTs, black) at the cell tips that drive oscillation of the associated spindle pole body (SPB, tan). These forces are transmitted to the centromeric heterochromatin.

(B) Nuclear envelope fluctuations are detected by 4D fluorescence microscopy. Fluorescence images of a wild-type *S. pombe* cell expressing the GFP fusion of nucleoporin Cut11; images are at the mid-plane of the nucleus in the z-dimension. At t = 0 (left), the nucleus is circular; ~55 seconds later (right), the same nucleus undergoes a MT-dependent deformation (arrowhead). Scale bar, 2 µm.

(C) Example of 3D nuclear reconstruction of the nucleus in (B) with sub-pixel resolution for precise fluctuation detection and measurement at t = 0 and t = 55s. The arrowhead indicates the region of the reconstructed fluctuation.

(D) Loss of Swi6 leads to larger nuclear surface deformations in response to MT dynamics. Representative single nuclear surface fluctuations shown as topological heat maps. Each nuclear surface is mapped with respect to its latitudinal angle (points above and below the nuclear "equator")—a band between +45 and -45 degrees is chosen to exclude less accurate fluctuation detection at the nuclear poles—and its longitudinal angle (points around the nucleus) between 0

and 360 degrees (Supp. Fig. S2). In the presence of microtubules (left column), a wild-type, *swi6Δ*, or *epe1Δ* nucleus exhibits deformations at distinct positions where the MTs impart the greatest shearing force during SPB oscillations. Without HP1-α/Swi6, the characteristic deformations enlarge, both in amplitude and nuclear surface area. Addition of MBC depolymerizes MTs and abolishes all large fluctuations across all genotypes (right column).

(E) Swi6 is associated with heterochromatic domains, which resides in distinct, regions of the nucleus and have unique properties. Schematic representation of a heterochromatin focus associated with the nuclear envelope (red). Nucleosomes (gray) are methylated on histone H3K9 (yellow) by the methyltransferase Suv39/Clr4 (orange). Upon methylation, the heterochromatin protein Swi6 (green) binds H3K9me, crosslinks adjacent nucleosomes, and condenses into a phase-separated domain to form compact heterochromatin (green region). The demethylase KDM2/Epe1 (purple) reverses this process, countering heterochromatin formation through H3K9me demethylation.

(F) Without Swi6, the scale of nuclear fluctuations increases. Hundreds of individual nuclei were reconstructed for each genotype, with the average, or root mean squared, population fluctuation size measured with respect to the cross-sectional nuclear radial angle (0 to 180 degrees). The characteristic fluctuation profile highlighting the predominant sites of MT-induced deformations at 45 and 135 degrees is preserved across genotypes (population mean, solid line; population standard deviations, band). As compared to wild-type nuclei (black, n = 207 nuclei), *swi6Δ* nuclei (green, n = 292 nuclei) exhibit larger fluctuations across all points on the nuclear surface, while *epe1Δ* nuclei (purple, n = 215 nuclei) show little change. The dotted line at 0.025 µm represents the lower limit of fluctuation detection.

(G) Global nuclear deformability increases without Swi6. Loss of HP1-α/Swi6 leads to enhanced root mean squared fluctuation size across all nuclear radial angles (left) and across all nuclei observed (middle and right). In the absence of MT dynamics (MBC-treated), the characteristic fluctuation profile of each nuclear population is abolished and shifted downwards (left), and the ensemble probability (middle) and cumulative probability (right) for fluctuation size is shifted toward smaller fluctuations (dashed lines; wt: n = 58 nuclei; *swi6Δ*: n = 69 nuclei; *epe1Δ*: n = 85 nuclei). Data are represented as mean (+/- SEM in left plot). Dotted line at 0.025 µm represents the lower limit of fluctuation detection.

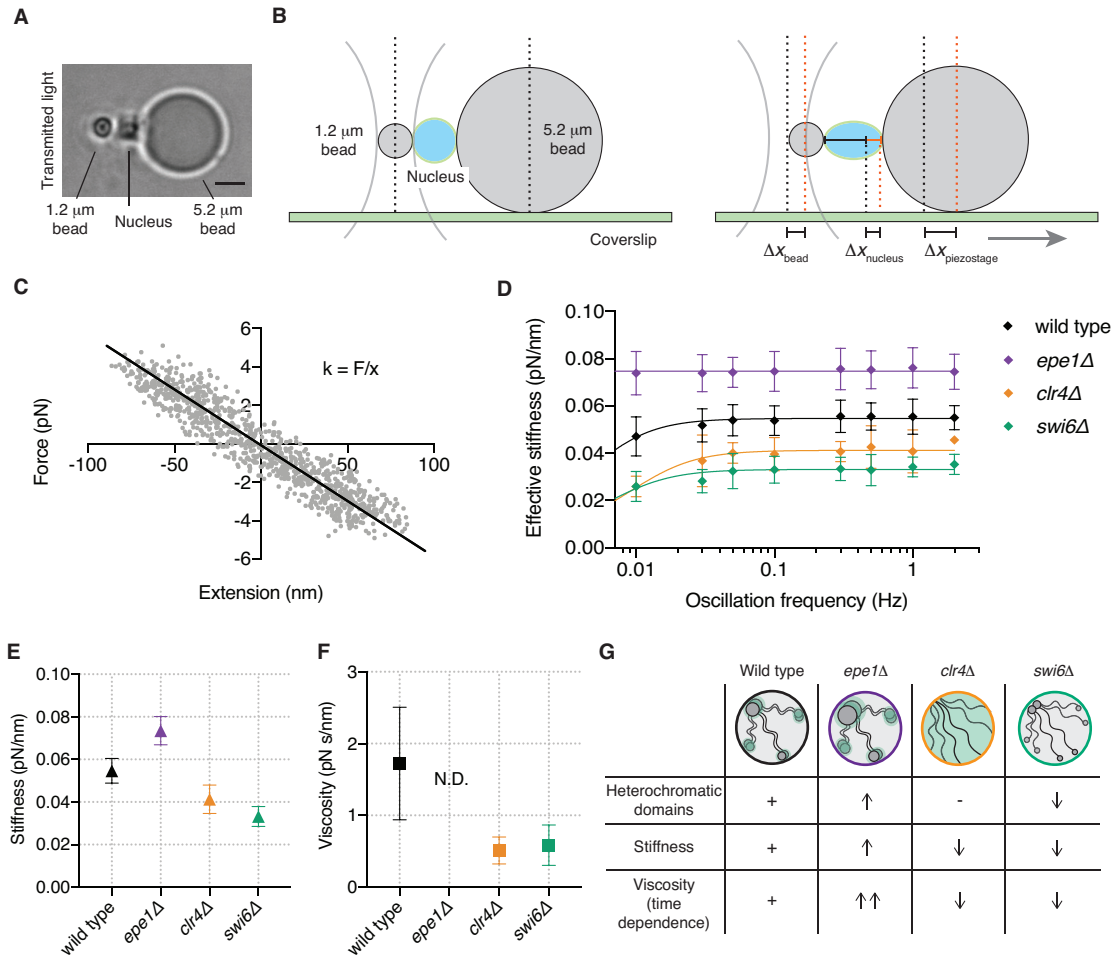

Figure 2. H3K9me-associated Swi6 strongly contributes to nuclear stiffness *in vitro*.
Loss of either H3K9me or Swi6 reduces the nuclear spring constant by half.
(A) Nuclear stiffness and viscosity is measured by force spectroscopy on an isolated nucleus. Transmitted light image showing the configuration as viewed from above. An isolated *S. pombe* nucleus expressing Cut11-GFP is sandwiched between two poly-ornithine-coated silica beads of differing sizes. Scale bar, 2 µm.
(B) Schematic representation of the force spectroscopy assay, where each nucleus is subjected to rounds of compression and tension. An isolated nucleus (light blue) is affixed to a 1.2 µm bead that is bound within an optical trap; the nucleus is affixed on its right side to a 5.2 µm bead adhered to a glass coverslip. The large bead and coverslip—attached to a piezostage—is respectively translated away and towards the optical trap by a pre-determined displacement ($\Delta x_{piezostage}$) to exert tension or compression on the sandwiched nucleus. The resulting displacement of the small bead in the optical trap (Δx_{bead}) is measured by its deflection of the trap infrared laser. The difference in the two displacements is equal to the displacement of the nucleus ($\Delta x_{nucleus}$).
(C) Each oscillation yields force and stiffness measurements. Representative force versus extension curve of an isolated wild-type nucleus. Each data point (gray) represents the force applied to the nucleus and the resulting displacement over one oscillation (extension and compression). The data display a linear relationship (black line); the slope (k) is equivalent to the spring constant, or effective stiffness, of the individual nucleus. Repeating oscillations at different frequencies can reveal the time-dependent (viscous) response (see Supp. Fig. S3).

(D) The nuclear force response is strongly responsive to manipulation of heterochromatic domains. As compared to wild-type nuclei (black, n = 8 nuclei; 63 oscillations), loss of KDM2/Epe1 increased the effective stiffness (purple, n = 18 nuclei; 172 oscillations), while loss of Suv39/Clr4 (orange, n = 3 nuclei; 22 oscillations) or HP1-α/Swi6 (green, n = 5 nuclei; 40 oscillations) decreases the effective stiffness over a range of oscillation frequencies (0.01 – 2 Hz). At lower frequencies, wild-type, *clr4Δ,* and *swi6Δ* nuclei exhibited a nonlinear mechanical response, characteristic of a viscoelastic material. To extract the individual elastic and viscous components, the frequency data was fit with a Maxwell viscoelastic model (solid lines). Data are represented as mean +/- SD of the raw oscillation data at each oscillation frequency.
(E) Nuclear stiffness depends on the presence and/or extent of heterochromatic domains. From the viscoelastic fits in (D), the nuclear stiffness was extracted for each genotype. As compared to wild-type mean stiffness (0.055 pN/nm), *epe1Δ* nuclei were stiffer (0.073 pN/nm), and *clr4Δ* and *swi6Δ* nuclei were softer (0.041 pN/nm and 0.033 pN/nm, respectively). Data are represented as mean +/- SD of the fitted values of data in (D).
(F) Nuclear viscosity depends on the presence and/or extent of heterochromatic domains. From the viscoelastic fits in (D), the nuclear viscosity was extracted for each genotype. As compared to wild-type viscosity (1.72 pN s/nm), *clr4Δ* and *swi6Δ* nuclei were significantly less viscous (0.51 pN s/nm and 0.58 pN s/nm, respectively). *epe1Δ* nuclei exhibit increased viscosity the magnitude of which could not be quantitatively determined due to lack of time dependence. Data are represented as mean +/- SD of the fitted values of data in (D).
(G) Schematic table representing the mechanical effects of altering H3K9me heterochromatic domains. When heterochromatin domains are enlarged, as in *epe1Δ* nuclei, the nuclear response to compression or tension force becomes less time-dependent, exhibiting both increased stiffness and viscosity. In contrast, when H3K9me heterochromatin domains are abolished (in *clr4Δ* nuclei) or altered (in *swi6Δ* nuclei), the nuclear response becomes more reactive (less time-dependent), with decreased nuclear stiffness and viscosity.

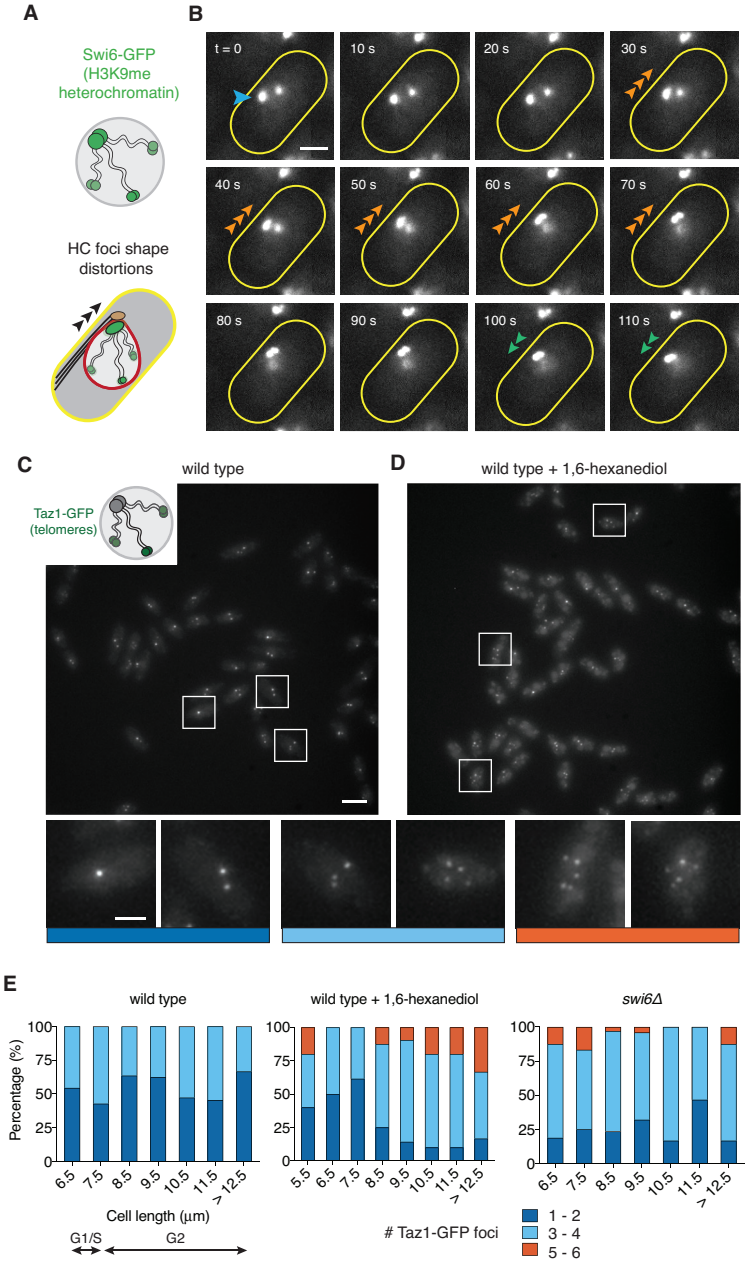

Figure 3. Heterochromatic domains exhibit liquid-like properties *in vivo* that promote telomere clustering.

(A) Schematic representation of the heterochromatin-domain fluorescence labeling assay. Swi6-GFP is expressed in cells to label H3K9me heterochromatin domains (light green).

(B) Heterochromatin domains are deformed in response to MT-driven nuclear oscillations. Time-lapse montage of cells expressing Swi6-GFP shows a large heterochromatin focus (blue arrowhead) transitioning from a round to an oblong shape that aligns with the long axis of the cell as it is translated in response to MT dynamics (orange arrowheads, t = 30 to t = 70 s). At t = 60 s, the focus begins to separate into two foci, and after MT dynamics resolve (t = 100 s), the focus coalesces and begins to translate back to its starting position (green arrowheads). Scale bar, 2 µm.

(C) Under normal conditions, the six fission yeast telomeres typically cluster into ~1-3 foci during interphase (boxes with magnifications below). Fluorescence maximum intensity projection of wild-type *S. pombe* cells expressing Taz1-GFP to label telomeres. Scale bars, 6 µm and 2 µm.
(D) Treatment of wild-type cells with 5% 1,6-hexanediol for 30 min leads to telomere de-clustering, as the number of Taz1-GFP foci increases to ~4-6 per nucleus (boxes with magnifications below).
(E) Swi6 is required for telomere clustering. Telomeres in cells lacking Swi6 de-cluster in a manner similar to hexanediol exposure. Percentage of cells containing Taz1-GFP foci; foci per cell were counted and grouped by cell length. In wild-type cells (n = 130), roughly half the population contained 1-2 (dark blue) or 3-4 (light blue) Taz1-GFP foci across the cell cycle. Upon exposure to 1,6-hexanediol (n = 135), Taz1-GFP foci number increased, particularly during G2, indicating telomere de-clustering. In cells lacking Swi6 (n = 150), telomere de-clustering relative to wild type cells was apparent.

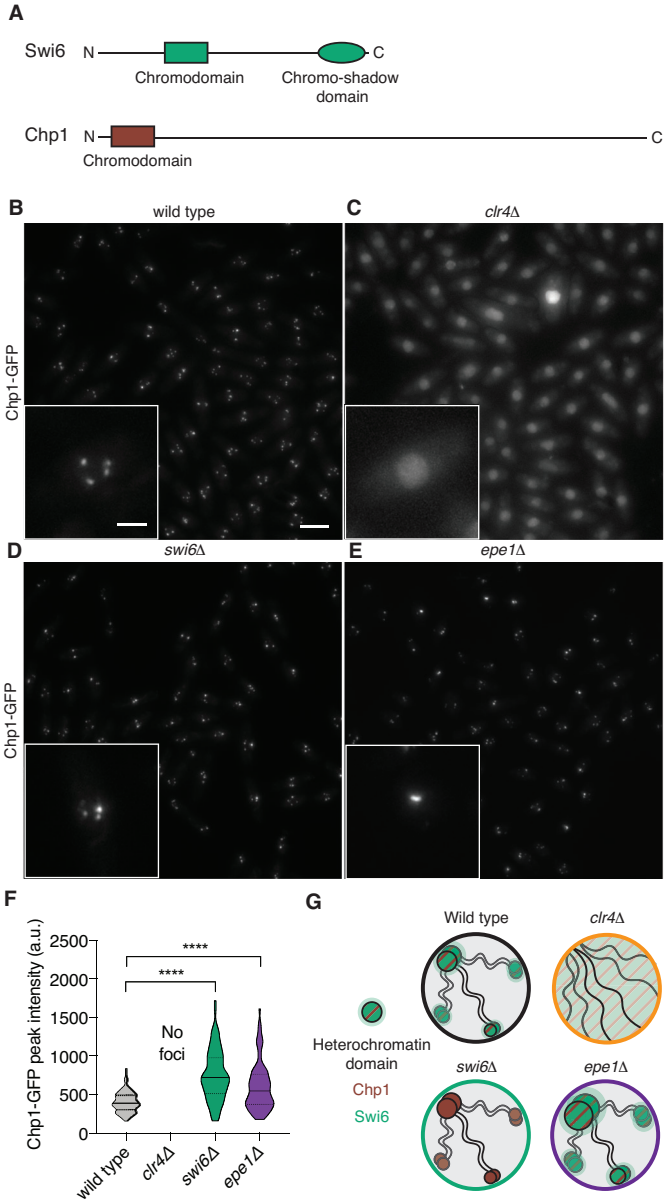

Figure 4. H3K9me binding proteins compete for binding sites in heterochromatic domains.
(A) Protein diagrams of the heterochromatin proteins in fission yeast, Swi6 and Chp1; drawn to scale. Swi6 (328 aa) consists of a chromodomain, chromo-shadow domain, and substantial N-terminal domain. In contrast, Chp1 (960 aa) contains only a chromodomain with a much smaller N-terminal domain.
(B) The relative recruitment of Chp1-GFP to heterochromatic domains is influenced by other heterochromatin binding proteins. Fluorescence maximum intensity projection of wild-type *S. pombe* cells expressing Chp1-GFP. Under normal conditions, Chp1 localizes to heterochromatin foci similar to Swi6 (Fig. 3). Scale bars, 6 µm and 2 µm.
(C) In the absence of Suv39/Clr4, H3K9me is abolished and Chp1-GFP becomes diffuse throughout the nucleus (inset).
(D) In cells lacking Swi6 expression, heterochromatic foci containing Chp1-GFP appear similar in number but are brighter (inset).

(E) When heterochromatin spreading becomes more permissive in *epe1Δ* cells, Chp1-GFP foci intensity increases, and numerous heterochromatin appear larger and elongated (inset).
(F) The recruitment of Chp1 to heterochromatic domains increases when competition from Swi6 is eliminated or when domains enlarge. Quantification of Chp1-GFP peak intensity for wild-type (n = 117 foci), *swi6Δ* (n = 91 foci), and *epe1Δ* (n = 84 foci) cells. **** $p < 0.0001$ by ordinary one-way ANOVA with Dunnett's multiple comparisons test.
(G) Schematic representation of H3K9me domains in each genotype. In wild-type cells, heterochromatic domains contain both Chp1 and Swi6. In *clr4Δ* cells, both Chp1 and Swi6 are delocalized. When Swi6 is removed, Chp1 can quantitatively bind heterochromatin to a greater extent, yet the increased presence of Chp1 is not sufficient to compensate for the mechanical role provided by Swi6. In the context of defective H3K9me demethylation (*epe1Δ*), heterochromatin domains enlarge, allowing for more heterochromatin to be bound by Chp1 (and Swi6).

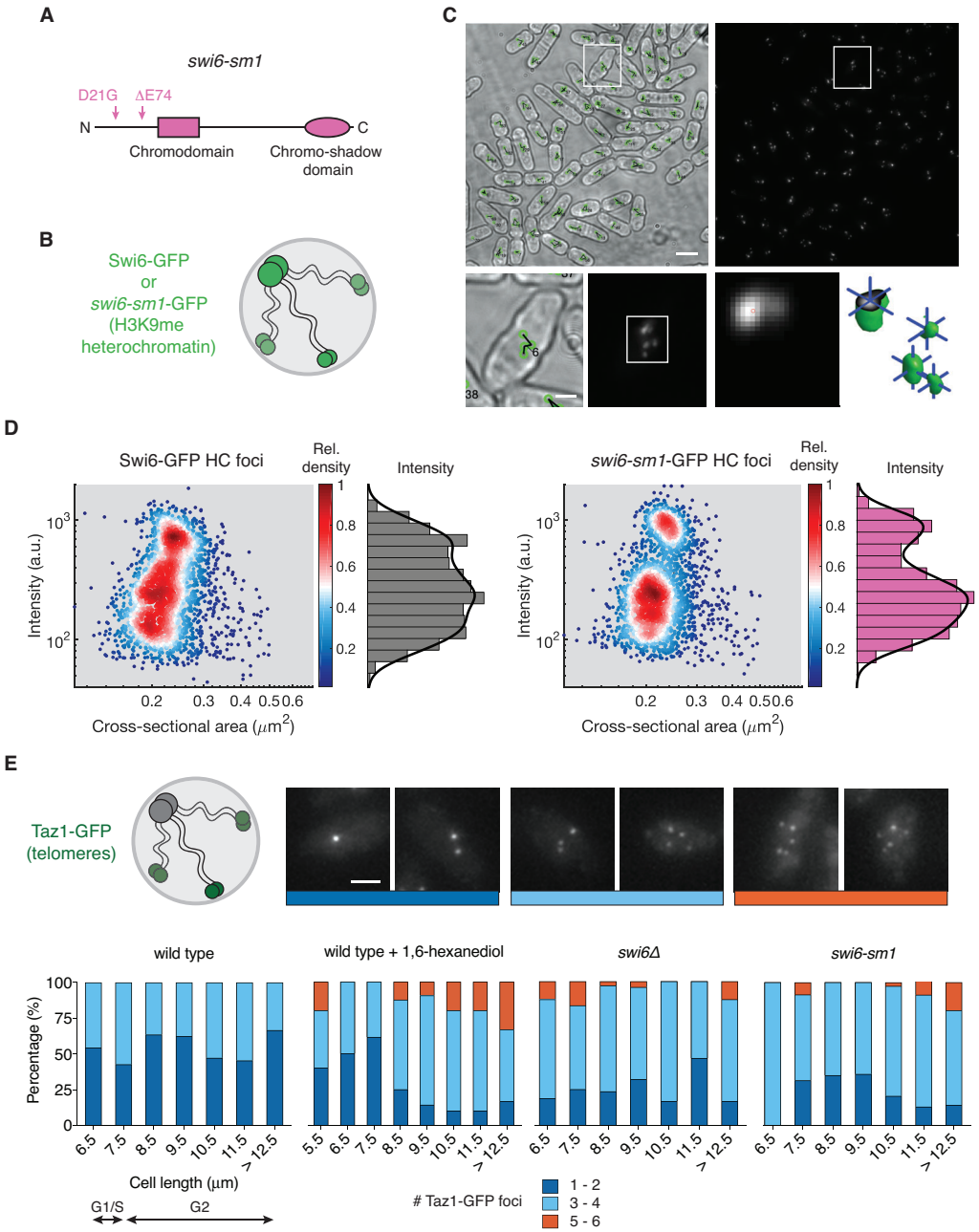

Figure 5. The *swi6-sm1* allele uncouples H3K9me binding from phase separation.
(A) Protein diagram representing the *swi6-sm1* allele with its two mutations in the N-terminal domain including D21G, which is in the recognition site for phosphorylation by casein kinase II.
(B) Schematic representation of the heterochromatin-domain fluorescence labeling assay. Swi6-GFP or *swi6-sm1*-GFP is expressed in cells to label H3K9me heterochromatin domains (light green).
(C) Heterochromatic domain size and intensity is measured using 3D domain reconstruction. Maximum intensity projections of transmitted light (upper left) and fluorescence images (upper right) of *S. pombe* cells expressing Swi6-GFP. Foci are grouped by cell (lower left) and individually reconstructed in three dimensions (lower right). Scale bars, 6 μm and 2 μm.

(D) The *swi6-sm1* allele leads to a depletion of intermediate scale and intensity heterochromatic domains relative to wild-type Swi6-GFP. Foci intensity versus cross-sectional area density scatter plots for Swi6-GFP (n = 2500 foci) and *swi6-sm1*-GFP (n = 2402 foci) labeled heterochromatin (HC) domains. Wild-type Swi6-GFP HC domains comprise a more uniform distribution of domain intensities spanning from bright (centromeric HC) to dim (telomeric and other HC) as shown by the corresponding histogram of foci intensities, while *swi6-sm1*-GFP expressing cells lack intermediate domains, consistent with a defect in clustering non-centromeric heterochromatin.
(E) The *swi6-sm1* allele leads to telomere de-clustering in a manner similar to hexanediol exposure and *swi6Δ*, suggesting that the liquid-like behavior of Swi6 that promotes telomere clustering is compromised by the *swi6-sm1* allele. Data expressed as (and replotted from) Figure 3E for wild-type cells with and without 1,6-hexanediol exposure and *swi6Δ* cells. In cells expressing *swi6-sm1* (n = 145), the de-clustering appeared similar to 1,6-hexanediol-treated cells or cells lacking Swi6.

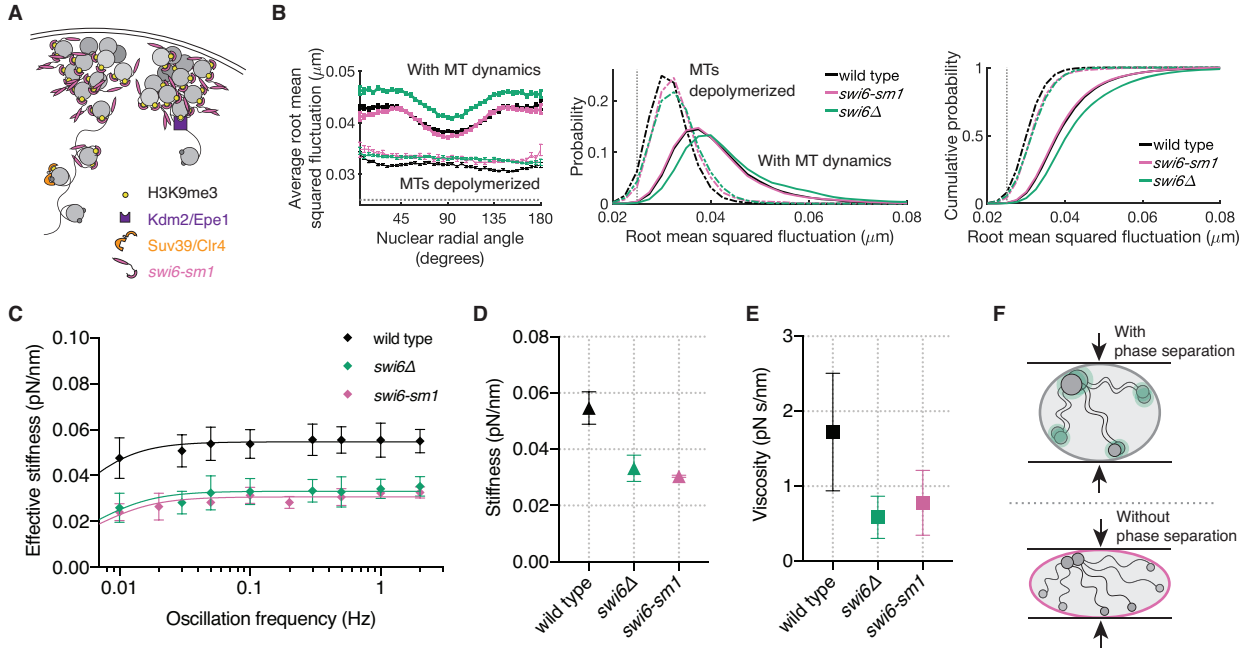

Figure 6. The *swi6-sm1* allele uncouples the mechanical defects of *swi6Δ* nuclei *in vivo* and *in vitro.*

(A) Schematic model for how expression of the *swi6-sm1* mutant influences H3K9me heterochromatic domains. Nucleosomes (gray) are methylated on histone H3K9 (yellow) by the methyltransferase Suv39/Clr4 (orange). Upon methylation, *swi6-sm1* (pink) binds H3K9me but cannot efficiently condense into a phase-separated domain, forming smaller, less compact heterochromatin.

(B) The *in vivo* mechanical response to MT dynamics remains intact in cells expressing *swi6-sm1*, likely due to its retained ability to support the centromeric functions including the recruitment of cohesion (Yamagishi et al., 2008). The average root mean squared population fluctuation size measured with respect to the cross-sectional nuclear angle (0 to 180 degrees) for wild-type (black, replotted from Fig. 1), *swi6Δ* (green, replotted from Fig. 1), and *swi6-sm1* (pink, n = 207 nuclei) nuclei (left). The characteristic fluctuation profile highlighting the predominant sites of MT-induced deformations is preserved across each genotype (population mean, solid line; population standard deviations, band). As compared to wild-type nuclei, *swi6-sm1* nuclei maintain the ability to resist MT-dependent deformations. In the absence of microtubules (MBC-treated/MTs depolymerized), the characteristic fluctuation profile of each nuclear population is abolished and shifted downwards (left), and the ensemble probability (middle) and cumulative probability (right) for fluctuation size is shifted toward smaller fluctuations (dashed lines; *swi6-sm1*: n = 36 nuclei). Without MT dynamics, *swi6-sm1* nuclei exhibited thermal fluctuation sizes similar to that observed for *swi6Δ* nuclei, suggesting a similar effect on global nuclear mechanics. Data are represented as mean (+/- SEM in left plot). Dotted line at 0.025 μm represents the lower limit of fluctuation detection.

(C) Isolated nuclei from cells expressing the *swi6-sm1* allele show similar mechanical defects to *swi6Δ* nuclei *in vitro*. Compared to wild-type nuclei (black, replotted from Fig. 2), both the complete loss of HP1-α/Swi6 (green, replotted from Fig. 2) or expression of the *swi6-sm1* variant (pink, n = 3 nuclei; 29 oscillations) decreased the effective nuclear stiffness over a range of oscillation frequencies (0.01 – 2 Hz). At lower frequencies, *swi6-sm1* nuclei also exhibited a nonlinear mechanical response, characteristic of a viscoelastic material. To extract the individual elastic

and viscous components, the frequency data was fit with a Maxwell viscoelastic model (solid lines). Data are represented as mean +/- SD of the raw oscillation data at each oscillation frequency.

(D) From the viscoelastic fits in (C), the actual nuclear stiffness was extracted for each genotype. As compared to wild-type mean stiffness (0.055 pN/nm), *swi6-sm1* nuclei were as soft (0.030 pN/nm) as *swi6Δ* nuclei (0.033 pN/nm). Wild-type and *swi6Δ* replotted from Fig. 2. Data are represented as mean +/- SD of the fitted values of data in (C).

(E) From the viscoelastic fits in (C), the nuclear viscosity was extracted for each genotype. As compared to wild-type viscosity (1.72 pN s/nm), *swi6-sm1* nuclei displayed similarly decreased viscosity (0.78 pN s/nm) as *swi6Δ* nuclei (0.58 pN s/nm). Wild-type and *swi6Δ* replotted from Fig. 2. Data are represented as mean +/- SD of the fitted values of data in (C).

(F) When Swi6 is able to form condensates as part of heterochromatic foci, these domains contribute both stiffness and viscosity to the nucleus, doing mechanical work for the nucleus as it resists compressive force (top). When this property is compromised, nuclear stiffness and viscosity are diminished and heterochromatin domains de-cluster (bottom).

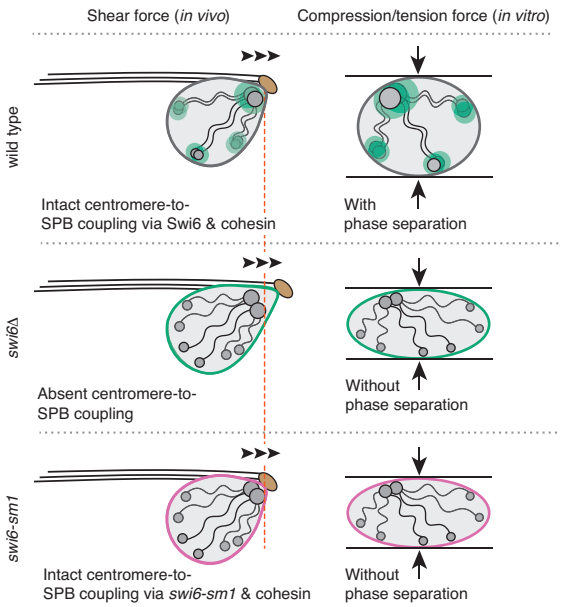

Figure 7. The ability of HP1-α/Swi6 to undergo LLPS is critical for nuclear resistance to compression and tension forces.

(top) In wild-type conditions, the nucleus has both (1) intact centromere cohesion that is engaged with the spindle pole body interface via Swi6 and cohesin, and (2) condensation of the heterochromatin-associated Swi6. The former mechanism predominantly contributes to resisting the shear forces driven *in vivo* by MT dynamics. The latter mechanism is able to resist direct compression and/or tension forces experienced *in vitro* (by yeast).

(middle) Without Swi6, centromere cohesion is compromised and is more weakly coupled to the spindle pole body, decreasing resistance to *in vivo* shearing forces due to MT dynamics. Without condensation of Swi6, the nucleus is less able to resist compression/tension forces and is softer and less viscous.

(bottom) The *swi6-sm1* allele decouples centromeric-SPB architecture defects from condensation of Swi6 through LLPS; intact centromere-to-SPB coupling via *swi6-sm1* and cohesin allows for a normal *in vivo* response to MT dynamics, while its inability to form LLPS domains results in an inability to resists direct compression and/or tension forces.

STAR Methods

RESOURCE AVAILABILITY

Lead Contact

Further information and requests for resources and reagents should be directed to and will be fulfilled by the Lead Contact, Megan King (megan.king@yale.edu).

Materials Availability

All unique/stable reagents and strains generated in this study are available from the Lead Contact without restriction.

Data and Code Availability

The code generated during this study (NuclearFluctuations, 3DMembraneReconstruction, and TweezersAnalysis) is available on GitHub at https://github.com/LusKingLab/.

EXPERIMENTAL MODEL AND SUBJECT DETAILS

Cell culture and strain generation

The strains used in this study is listed in Supplementary Table 1. *S. pombe* cells were grown and maintained in standard cell culture conditions at 30°C (Moreno et al., 1991). Gene replacements were made by replacement of the open reading frames with the kanMX6 (Bähler et al., 1998), hphMX6, or natMX6 cassettes (Hentges et al., 2005). C- and N-terminal GFP tagging was performed with pFa6a-GFP-kanMX6 (Bähler et al., 1998); the pFa6a-mCherry-kanMX6 cassette was used as a template for C-terminal mCherry tagging (Snaith et al., 2005). All strains generated by cassette integration were confirmed by PCR. Strains made through genetic crosses were confirmed by the

segregation of selection markers and/or by the presence of the designated fluorescently-tagged protein.

METHOD DETAILS

Microscopy

S. pombe strains were grown in YE5S plus 250 mg/L adenine to log phase (OD_{600} 0.5-0.8). Cells were mounted on agarose pads (1.4% agarose in EMM5S) and sealed with VALAP (1:1:1, vaseline:lanolin:paraffin). Cells treated with MBC were incubated on agar pads with 50 mg/mL MBC for 10 min before imaging. Cells treated with 1,6-hexanediol were incubated with final concentrations of 5% 1,6-hexanediol for 15 or 30 min and imaged directly thereafter. Live-cell images were acquired on a Deltavision Widefield Deconvolution Microscope (Applied Precision/GE Healthcare) with a CoolSnap HQ2 CCD camera (Photometrics) or an Evolve 512 EMCCD camera (Photometrics). For nuclear contour imaging, 10 z-slices with 20-ms exposure time and 400-nm spacing were taken every 2.5 s for 5 min with the EMCCD camera. For GFP-Swi6 imaging, 20 z-slices with 0.1-sec exposure time and 200-nm spacing with taken with the EMCCD camera. For Swi6-GFP time-lapse imaging, single mid-plane z-slices with 0.15-sec exposure time were taken every 5 sec with the CCD camera. For telomere/Taz1-GFP imaging, 15 z-slices with 50-ms exposure time and 320-nm spacing were taken with the EMCCD camera. For Chp1-GFP imaging, 20 z-slices with 0.2-sec exposure time and 200-nm spacing were taken with the CCD camera. For Swi6/Swi6-sm1-mCherry imaging, 16 z-slices with 10-ms exposure time and 400-nm spacing with taken with the EMCCD camera.

Nuclear isolation

Nuclei were isolated using a protocol previously described in (Schreiner et al., 2015). Briefly, strains were grown to log phase in rich media (YE5S) at 30°C and diluted into 1 liter YE5S for overnight growth. Cells were harvested the following day at an OD_{600} ~0.8 and incubated in 100 mM Tris pH 9.4 and 10 mM DTT for 10 min at 33°C to prepare for spheroplasting. Cells were spheroplasted in 0.4 mg/mL zymolase (MP Biomedicals), 0.6 mg/mL lysing enzymes (Sigma), 350 μL beta-glucuronidase (MP Biomedicals) and 5 mM DTT in 1.1 M sorbitol at 33°C for 2-3 hours. Spheroplasts (nuclei) were isolated from cells by centrifugation using a series of three density-step sucrose gradients, and aliquots were flash frozen in liquid N_2 and stored at -80°C. To thaw for use, one aliquot was dialyzed overnight in 500 mL dialysis buffer (80 mM PIPES, 5% DMSO, 2 mM $MgCl_2$, 1 mM EGTA, 500 mM sucrose).

Force spectroscopy oscillation assay

Force spectroscopy was performed on isolated nuclei as previously described in (Schreiner et al., 2015). In a flow cell, isolated *S. pombe* nuclei were trapped and fixed via electrostatic interactions to poly-ornithine-coated silica beads by micromanipulation using optical tweezers. Optical trapping and interferometry position detection was achieved using a single-beam gradient focus from a 3-watt 1064 nm ND:YAG laser. The focused laser was used to trap beads and nuclei within the flow cell, which was mounted onto a piezo-controlled stage with nanometer precision. To visualize each nucleus, an epifluorescence microscope was coupled with the optical tweezers, equipped with a 470 nm excitation source (blue light emitting diode). Each nucleus was attached to the side of an immobilized bead, which elevated the nucleus off the coverslip and provided a stationary structure upon which forces can be applied. Next, a smaller bead was fixed to the free side of the nucleus, creating a bead-nucleus-bead sandwich. While holding the smaller bead within the trap, the coverslip was then moved back and forth in the x-direction; the large bead, which was fixed to the coverslip transmitted this force to the nucleus as either tension (pulling away) or compression

(pushing towards). To exert compression and tension forces, the stage was driven sinusoidally with an amplitude range of 60-100 nm (physiologic length scales), at discrete frequencies of 0.01-2 Hz. As the stage was driven, the affixed large bead transmitted force directly to the nucleus, which in turn, transmitted a force proportional to the stiffness of the nucleus to the smaller bead in the optical trap. Movement of the smaller, trapped bead was detected using back focal plane interferometry via an infrared-enhanced quadrant photodiode, and the difference between the movement of the smaller, trapped bead and the larger bead fixed to the stage was equal to the change in nuclear shape along the axis of movement, i.e., how much the nucleus was being compressed or extended.

QUANTIFICATION AND STATISTICAL ANALYSIS

Statistical details (statistical tests used, exact value for n, what n represents, definition of center, and dispersion and precision of measures) for each experiment can be found in the figure legends. Microsoft Excel was used to tabulate values, Prism was used to create simple plots (Fig. 2D, E, F; Fig. 3E; Fig. 4F; Fig. 5E; Fig. 6C, D, E), and MATLAB was used for all other analysis and plotting. * $p < 0.05$; ** $p < 0.01$; *** $p < 0.001$; **** $p < 0.0001$ by ordinary one-way ANOVA with Dunnett's multiple comparisons test or unpaired t-test.

Nuclear fluctuation analysis

Nuclear envelope contour fitting and fluctuation time analysis were performed as previously described in (Schreiner et al., 2015) and (Zhao et al., 2016). Briefly, our contour fitting algorithm reconstructed the three-dimensional nuclear shape with sub-pixel resolution from a z-stack of 10 two-dimensional images by maximizing the total intensity of the nuclear envelope across the z-stack and minimizing the nuclear

envelope's total curvature. To minimize the effects of aberration and difficulties with image noise at the nuclear caps in the z-dimension, we limited our fluctuation analysis to a band 45 degrees above and below the center/"equator" of the nucleus (Fig. 1D). Each fluctuation was detected by comparing its radial distance from the nuclear center to a time-averaged radial distance at that same position. The average, or root mean squared, fluctuation size was calculated according to:

$$RMSF(\theta,\varphi) = \frac{1}{T}\sum_{t=1}^{T}\sqrt{(r(\theta,\varphi,t) - \langle r(\theta,\varphi,t)\rangle_t)^2}$$

Where T is the total number of frames, $r(\theta, \varphi, t)$ is the radial distance from the nuclear center at vertex angle (θ, φ) at frame t and $< r(\theta, \varphi, t) >_t$ denotes the time-averaged radial distance. Individual fluctuations were tracked over time using 2D particle tracking, assigning longer fluctuations (> 10 frames/25 s) to those induced by microtubules and shorter fluctuations arising from baseline thermal activity. Peak height, formation (rise) time, and resolution (decay) time were determined by fitting each fluctuation trajectory to a single, asymmetric triangle waveform.

Force spectroscopy data analysis

To determine the effective stiffness of the nucleus ($k_{nucleus}$), the system was treated as a spring that adheres to Hooke's law ($F = k_{nucleus}\Delta_{nucleus}$), where $\Delta_{nucleus}$ is the displacement of the nucleus (either in extension or compression) and F is the force imparted to the nucleus from the oscillating stage. $\Delta_{nucleus}$ was calculated as the difference between the piezo stage displacement ($\Delta_{piezostage}$) and the displacement of the small bead from the center of the trap (Δ_{trap}). The force F on the nucleus is equal and opposite to the force on the bead in the trap, therefore determining the stiffness of the trap allowed us to calculate the force acting upon the bead and thus the force acting upon the nucleus. The inherent stiffness of the optical trap was determined for each

experiment by fitting the power spectral density of a trapped 1.2 μm bead to a Lorentzian function to extract the corner frequency (Mack et al., 2012). The trap stiffness is the ratio of this corner frequency to the bead's friction coefficient. We subjected each nucleus to multiple rounds of compression and extension at different frequencies (0.01 – 2 Hz), enabling us to observe any time-dependent mechanical properties. We then fit the effective stiffness data with a Maxwell viscoelastic model to extract the elastic (spring) and viscous (dashpot/dampener) components, K and η respectively, using the corresponding fitting function for the effective stiffness:

$$k(f) = \frac{2\pi K\eta f}{\sqrt{(2\pi\eta f)^2 + K^2}}$$

Telomere imaging and analysis

Only live, nonmitotic cells that had completed cytokinesis were considered for Taz1-GFP and cell length analysis. Maximum intensity projections were displayed as described in the figure legends. Images were analyzed in ImageJ (Fiji; (Schindelin et al., 2012). To calculate the number of Taz1-GFP foci per cell, maximum Z-projections were generated and total number of Taz1-GFP foci per cell were counted.

Three-dimensional heterochromatin foci analysis

GFP-Swi6, Swi6-GFP, and *swi6-sm1*-GFP cross-sectional foci areas and intensities were measured using three-dimensional reconstructions of GFP foci with a custom MATLAB software previously described (Zhao et al., 2016). Foci were grouped by cell using a minimum separation distance of 40-50 pixels from the center of the grouping; this adequately grouped together foci of the same nucleus while excluding foci from nearby, neighboring cells. Z-stack images for each focus were individually fit with a

three-dimensional Gaussian function to determine maximum focus width in both x and y-dimensions as well as foci integrated intensity. Foci intensity vs. cross-sectional area plots and histograms were generated using the MATLAB functions dscatter (Eilers and Goeman, 2004) and scatterhist.

References

Alberti, S., Gladfelter, A., and Mittag, T. (2019). Considerations and Challenges in Studying Liquid-Liquid Phase Separation and Biomolecular Condensates. Cell *176*, 419–434.

Allshire, R.C., Nimmo, E.R., Ekwall, K., Javerzat, J.P., and Cranston, G. (1995). Mutations derepressing silent centromeric domains in fission yeast disrupt chromosome segregation. Genes Dev. *9*, 218–233.

Bähler, J., Wu, J.Q., Longtine, M.S., Shah, N.G., Mckenzie, A., III, Steever, A.B., Wach, A., Philippsen, P., and Pringle, J.R. (1998). Heterologous modules for efficient and versatile PCR-based gene targeting in Schizosaccharomyces pombe. Yeast *14*, 943–951.

Bickmore, W.A., and van Steensel, B. (2013). Genome Architecture: Domain Organization of Interphase Chromosomes. Cell *152*, 1270–1284.

Brangwynne, C.P., Mitchison, T.J., and Hyman, A.A. (2011). Active liquid-like behavior of nucleoli determines their size and shape in Xenopus laevis oocytes. Pnas *108*, 4334–4339.

Bustin, M., and Misteli, T. (2016). Nongenetic functions of the genome. Science *352*, aad6933–aad6933.

Canzio, D., Chang, E.Y., Shankar, S., Kuchenbecker, K.M., Simon, M.D., Madhani, H.D., Narlikar, G.J., and Al-Sady, B. (2011). Chromodomain-mediated oligomerization

of HP1 suggests a nucleosome-bridging mechanism for heterochromatin assembly. Mol. Cell *41*, 67–81.

Canzio, D., Liao, M., Naber, N., Pate, E., Larson, A., Wu, S., Marina, D.B., Garcia, J.F., Madhani, H.D., Cooke, R., et al. (2013). A conformational switch in HP1 releases auto-inhibition to drive heterochromatin assembly. Nature *496*, 377–381.

Cooper, J.P., Watanabe, Y., and Nurse, P. (1998). Fission yeast Taz1 protein is required for meiotic telomere clustering and recombination. Nature *392*, 828–831.

Damodaran, K., Venkatachalapathy, S., Alisafaei, F., Radhakrishnan, A.V., Sharma Jokhun, D., Shenoy, V.B., and Shivashankar, G.V. (2018). Compressive force induces reversible chromatin condensation and cell geometry dependent transcriptional response. Mol. Biol. Cell mbcE18040256.

Denais, C.M., Gilbert, R.M., Isermann, P., McGregor, A.L., Lindert, te, M., Weigelin, B., Davidson, P.M., Friedl, P., Wolf, K., and Lammerding, J. (2016). Nuclear envelope rupture and repair during cancer cell migration. Science *352*, 353–358.

Eilers, P.H.C., and Goeman, J.J. (2004). Enhancing scatterplots with smoothed densities. Bioinformatics *20*, 623–628.

Ekwall, K., Javerzat, J.P., Lorentz, A., Schmidt, H., Cranston, G., and Allshire, R. (1995). The chromodomain protein Swi6: a key component at fission yeast centromeres. Science *269*, 1429–1431.

Erdel, F., Rademacher, A., Vlijm, R., Tünnermann, J., Frank, L., Weinmann, R., Schweigert, E., Yserentant, K., Hummert, J., Bauer, C., et al. (2020). Mouse Heterochromatin Adopts Digital Compaction States without Showing Hallmarks of HP1-Driven Liquid-Liquid Phase Separation. Mol. Cell *78*, 236–249.e237.

Falk, M., Feodorova, Y., Naumova, N., Imakaev, M., Lajoie, B.R., Leonhardt, H., Joffe, B., Dekker, J., Fudenberg, G., Solovei, I., et al. (2019). Heterochromatin drives compartmentalization of inverted and conventional nuclei. Nature *570*, 395–399.

Furusawa, T., Rochman, M., Taher, L., Dimitriadis, E.K., Nagashima, K., Anderson, S., and Bustin, M. (2015). Chromatin decompaction by the nucleosomal binding protein HMGN5 impairs nuclear sturdiness. Nat Commun *6*, 6138.

Gasser, S.M., Hediger, F., Taddei, A., Neumann, F.R., and Gartenberg, M.R. (2004). The function of telomere clustering in yeast: the circe effect. Cold Spring Harb. Symp. Quant. Biol. *69*, 327–337.

Gonzalez-Sandoval, A., and Gasser, S.M. (2016). Mechanism of chromatin segregation to the nuclear periphery in C. elegans embryos. Worm *5*, e1190900.

Haldar, S., Saini, A., Nanda, J.S., Saini, S., and Singh, J. (2011). Role of Swi6/HP1 self-association-mediated recruitment of Clr4/Suv39 in establishment and maintenance of heterochromatin in fission yeast. J. Biol. Chem. *286*, 9308–9320.

Harada, T., Swift, J., Irianto, J., Shin, J.-W., Spinler, K.R., Athirasala, A., Diegmiller, R., Dingal, P.C.D.P., Ivanovska, I.L., and Discher, D.E. (2014). Nuclear lamin stiffness is a barrier to 3D migration, but softness can limit survival. J. Cell Biol. *204*, 669–682.

Hatch, E.M., and Hetzer, M.W. (2016). Nuclear envelope rupture is induced by actin-based nucleus confinement. J. Cell Biol. *215*, 27–36.

Hentges, P., Van Driessche, B., Tafforeau, L., Vandenhaute, J., and Carr, A.M. (2005). Three novel antibiotic marker cassettes for gene disruption and marker switching in Schizosaccharomyces pombe. Yeast *22*, 1013–1019.

Kanoh, J., Sadaie, M., Urano, T., and Ishikawa, F. (2005). Telomere Binding Protein Taz1 Establishes Swi6 Heterochromatin Independently of RNAi at Telomeres. Curr. Biol. *15*, 1808–1819.

King, M.C., Drivas, T.G., and Blobel, G. (2008). A network of nuclear envelope membrane proteins linking centromeres to microtubules. Cell *134*, 427–438.

Lammerding, J., Fong, L.G., Ji, J.Y., Reue, K., Stewart, C.L., Young, S.G., and Lee, R.T. (2006). Lamins A and C but not lamin B1 regulate nuclear mechanics. J. Biol. Chem. *281*, 25768–25780.

Larson, A.G., and Narlikar, G.J. (2018). The Role of Phase Separation in Heterochromatin Formation, Function, and Regulation. Biochemistry *57*, 2540–2548.

Larson, A.G., Elnatan, D., Keenen, M.M., Trnka, M.J., Johnston, J.B., Burlingame, A.L., Agard, D.A., Redding, S., and Narlikar, G.J. (2017). Liquid droplet formation by HP1α suggests a role for phase separation in heterochromatin. Nature *547*, 236–240.

Lorentz, A., Ostermann, K., Fleck, O., and Schmidt, H. (1994). Switching gene swi6, involved in repression of silent mating-type loci in fission yeast, encodes a homologue of chromatin-associated proteins from Drosophila and mammals. Gene *143*, 139–143.

Lusk, C.P., and King, M.C. (2017). The nucleus: keeping it together by keeping it apart. Current Opinion in Cell Biology *44*, 44–50.

Mack, A.H., Schlingman, D.J., Regan, L., and Mochrie, S.G.J. (2012). Practical axial optical trapping. Rev Sci Instrum *83*, 103106.

Moreno, S., Klar, A., and Nurse, P. (1991). Molecular genetic analysis of fission yeast Schizosaccharomyces pombe. Meth. Enzymol. *194*, 795–823.

Nakayama, J.-I., Allshire, R.C., Klar, A.J.S., and Grewal, S.I.S. (2001). A role for DNA polymerase α in epigenetic control of transcriptional silencing in fission yeast. Embo J. *20*, 2857–2866.

Probst, A.V., and Almouzni, G. (2008). Pericentric heterochromatin: dynamic organization during early development in mammals. Differentiation *76*, 15–23.

Raab, M., Gentili, M., de Belly, H., Thiam, H.R., Vargas, P., Jimenez, A.J., Lautenschlaeger, F., Voituriez, R., Lennon-Duménil, A.M., Manel, N., et al. (2016). ESCRT III repairs nuclear envelope ruptures during cell migration to limit DNA damage and cell death. Science *352*, 359–362.

Rosowski, K.A., Sai, T., Vidal-Henriquez, E., Zwicker, D., Style, R.W., and Dufresne, E.R. (2020). Elastic ripening and inhibition of liquid–liquid phase separation. Nature Physics *16*, 422–425.

Sadaie, M., Iida, T., Urano, T., and Nakayama, J.-I. (2004). A chromodomain protein, Chp1, is required for the establishment of heterochromatin in fission yeast. Embo J. *23*, 3825–3835.

Sadaie, M., Kawaguchi, R., Ohtani, Y., Arisaka, F., Tanaka, K., Shirahige, K., and Nakayama, J.-I. (2008). Balance between distinct HP1 family proteins controls heterochromatin assembly in fission yeast. Mol. Cell. Biol. *28*, 6973–6988.

Schindelin, J., Arganda-Carreras, I., Frise, E., Kaynig, V., Longair, M., Pietzsch, T., Preibisch, S., Rueden, C., Saalfeld, S., Schmid, B., et al. (2012). Fiji: an open-source platform for biological-image analysis. Nat. Methods *9*, 676–682.

Schreiner, S.M., Koo, P.K., Zhao, Y., Mochrie, S.G.J., and King, M.C. (2015). The tethering of chromatin to the nuclear envelope supports nuclear mechanics. Nat Commun *6*, 7159.

Shah, P., Wolf, K., and Lammerding, J. (2017). Bursting the Bubble - Nuclear Envelope Rupture as a Path to Genomic Instability? Trends Cell Biol. *27*, 546–555.

Shimada, A., Dohke, K., Sadaie, M., Shinmyozu, K., Nakayama, J.-I., Urano, T., and Murakami, Y. (2009). Phosphorylation of Swi6/HP1 regulates transcriptional gene silencing at heterochromatin. Genes Dev. *23*, 18–23.

Shin, Y., Chang, Y.-C., Lee, D.S.W., Berry, J., Sanders, D.W., Ronceray, P., Wingreen, N.S., Haataja, M., and Brangwynne, C.P. (2018). Liquid Nuclear Condensates Mechanically Sense and Restructure the Genome. Cell *175*, 1481–1491.e13.

Snaith, H.A., Samejima, I., and Sawin, K.E. (2005). Multistep and multimode cortical anchoring of tea1p at cell tips in fission yeast. Embo J. *24*, 3690–3699.

Stephens, A.D., Banigan, E.J., Adam, S.A., Goldman, R.D., and Marko, J.F. (2017). Chromatin and lamin A determine two different mechanical response regimes of the cell nucleus. Mol. Biol. Cell *28*, 1984–1996.

Stephens, A.D., Liu, P.Z., Banigan, E.J., Almassalha, L.M., Backman, V., Adam, S.A., Goldman, R.D., and Marko, J.F. (2018). Chromatin histone modifications and rigidity affect nuclear morphology independent of lamins. Mol. Biol. Cell *29*, 220–233.

Strom, A.R., Emelyanov, A.V., Mir, M., Fyodorov, D.V., Darzacq, X., and Karpen, G.H. (2017). Phase separation drives heterochromatin domain formation. Nature *547*, 241–245.

Style, R.W., Sai, T., Fanelli, N., Ijavi, M., Smith-Mannschott, K., Xu, Q., Wilen, L.A., and Dufresne, E.R. (2018). Liquid-Liquid Phase Separation in an Elastic Network. Phys. Rev. X *8*, 011028.

Towbin, B.D., Gonzalez-Sandoval, A., and Gasser, S.M. (2013). Mechanisms of heterochromatin subnuclear localization. Trends in Biochemical Sciences *38*, 356–363.

Vargas, J.D., Hatch, E.M., Anderson, D.J., and Hetzer, M.W. (2012). Transient nuclear envelope rupturing during interphase in human cancer cells. Nucleus *3*, 88–100.

Wang, J., Reddy, B.D., and Jia, S. (2015). Rapid epigenetic adaptation to uncontrolled heterochromatin spreading. eLife *4*, 80.

Weaire, D.L., and Hutzler, S. (1999). The Physics of Foams.

Weinbreck, F., Minor, M., and de Kruif, C.G. (2008). Microencapsulation of oils using whey protein/gum arabic coacervates. Journal of Microencapsulation *21*, 667–679.

Yamagishi, Y., Sakuno, T., Shimura, M., and Watanabe, Y. (2008). Heterochromatin links to centromeric protection by recruiting shugoshin. Nature *455*, 251–255.

Yamanaka, S., Mehta, S., Reyes-Turcu, F.E., Zhuang, F., Fuchs, R.T., Rong, Y., Robb, G.B., and Grewal, S.I.S. (2013). RNAi triggered by specialized machinery silences developmental genes and retrotransposons. Nature *493*, 557–560.

Zhang, H., Zhao, R., Tones, J., Liu, M., Dilley, R., Chenoweth, D.M., Greenberg, R.A., and Lampson, M.A. (2020). Nuclear body phase separation drives telomere clustering in ALT cancer cells. Mol. Biol. Cell mbcE19100589.

Zhao, Y., Schreiner, S.M., Koo, P.K., Colombi, P., King, M.C., and Mochrie, S.G.J. (2016). Improved Determination of Subnuclear Position Enabled by Three-Dimensional Membrane Reconstruction. Biophys. J. *111*, 19–24.

Zofall, M., and Grewal, S.I.S. (2006). Swi6/HP1 Recruits a JmjC Domain Protein to Facilitate Transcription of Heterochromatic Repeats. Mol. Cell *22*, 681–692.